

BIOPHYSICS

An Omni-Mesoscope for multiscale high-throughput quantitative phase imaging of cellular dynamics and high-content molecular characterization

Hongqiang Ma^{1,2,*}, Maomao Chen¹, Jianquan Xu¹, Yixin Yang², Yongxin Zhao^{3,4}, Yang Liu^{1,2,5,*}

The mesoscope has emerged as a powerful imaging tool in biomedical research, yet its high cost and low resolution have limited its broader application. Here, we introduce the Omni-Mesoscope, a high-spatial-temporal and multimodal mesoscopic imaging platform built from cost-efficient off-the-shelf components. This system uniquely merges the capabilities of label-free quantitative phase microscopy to capture live-cell morphodynamics across thousands of cells with highly multiplexed fluorescence imaging for comprehensive molecular characterization. This Omni-Mesoscope offers a mesoscale field of view of ~5 square millimeters with a high spatial resolution down to 700 nanometers, enabling the capture of detailed subcellular features. We demonstrate its capability in delineating molecular characteristics underlying rare morphodynamic cellular phenomena, including cancer cell responses to chemotherapy and the emergence of polyploidy in drug-resistant cells. We also integrate expansion technique to enhance three-dimensional volumetric super-resolution imaging of thicker tissues, opening the avenues for biological exploration at unprecedented scales and resolutions.

INTRODUCTION

Biological systems are characterized by substantial cellular and molecular heterogeneity, functioning within diverse microenvironments across various timescales (1, 2). Addressing this complexity requires technologies capable of simultaneously capturing both the behaviors and molecular characteristics of individual cells over time across a large cell population in their spatial context at a high temporal and spatial resolution. Such a high-throughput high-resolution imaging system is crucial for identifying dynamic, rare events coupled with detailed subcellular and molecular characteristics, thereby facilitating in-depth analysis of diverse cellular phenotypes. This multiscale multifunctional imaging approach is crucial in revealing the mechanisms underlying therapeutic response from a systems-to-molecular perspective and in identifying effective diagnostic or prognostic biomarkers.

Traditional imaging systems are often limited by a compromise between the field of view (FOV) and image resolution, significantly hindering our ability to simultaneously observe cellular dynamics with the necessary subcellular details across a large cell population. The emergence of mesoscopic imaging technology represents a significant advancement, offering an ultralarge FOV spanning several millimeters (3). However, most mesoscopic systems are limited to a resolution of several micrometers (4–10) because of various factors such as numerical aperture (NA), optical aberrations, magnification, and image sensors. Although existing mesoscope allows us to observe cell dynamics over a large cell population, their limited resolution hampers the visualization of the subcellular details. To enhance spatial resolution, specially designed mesoscopic objective lenses

with a higher NA (up to 0.47) [e.g., mesolens (11)] have been developed, along with camera/detector arrays (12, 13) to increase the curved FOV, but their widespread adoption is hindered by the complexity and cost of manufacturing. Moreover, a conventional mesoscope often relies on a few fluorescent markers, which can perturb the natural state of cells, thus limiting the capacity for long-term observation of live-cell dynamics with rich functional insights. These challenges underscore the urgent need for an advanced multimodal imaging solution that can overcome these limitations to observe cell dynamics at a high spatiotemporal resolution over a large cell population without sacrificing in-depth functional information.

We present the Omni-Mesoscope, a versatile and cost-effective multimodal mesoscopic imaging system that achieves a submicrometer spatial resolution across a wide FOV, ~5 mm², at a speed of 4 frames per second, primarily limited by the camera speed. Omni-Mesoscope couples quantitative phase microscopy for label-free live-cell imaging with highly multiplex fluorescence microscopy for high-content functional imaging. This integration allows for continuous monitoring of live-cell dynamics alongside detailed molecular analysis on the same cells over a large cell population, providing a comprehensive view of large-scale dynamic cellular processes and their underlying molecular characteristics. We demonstrate the capability of Omni-Mesoscope to identify rare cell behaviors in response to chemotherapy drugs, which are linked to their underlying molecular characteristics. Furthermore, by incorporating expansion microscopy, we demonstrate the potential of Omni-Mesoscope for three-dimensional (3D) volumetric super-resolution imaging of thick tissue across the mesoscale. This imaging system not only overcomes the limitations of conventional techniques but also opens avenues for exploring the complexities of biological systems at unprecedented scales and resolutions.

RESULTS

Configuration and performance evaluation of the Omni-Mesoscope

Our Omni-Mesoscope is an automated imaging system with two major imaging modalities: label-free quantitative phase imaging

Copyright © 2024 The Authors, some rights reserved; exclusive licensee American Association for the Advancement of Science. No claim to original U.S. Government Works. Distributed under a Creative Commons Attribution NonCommercial License 4.0 (CC BY-NC).

¹Departments of Medicine and Bioengineering, University of Pittsburgh, Pittsburgh, PA 15213, USA. ²Department of Bioengineering, Beckman Institute for Advanced Science and Technology, University of Illinois Urbana-Champaign, Urbana, IL 61801, USA. ³Departments of Biological Sciences and Biomedical Engineering, Carnegie Mellon University, Pittsburgh, PA 15213, USA. ⁴Viron Molecular Medicine Institute, Boston, MA 02201, USA. ⁵Departments of Bioengineering and Electrical and Computer Engineering, Beckman Institute for Advanced Science and Technology, Cancer Center at Illinois, University of Illinois Urbana-Champaign, Urbana, IL 61801, USA.

*Corresponding author. Email: mhq@illinois.edu (H.M.); liuy46@illinois.edu (Y.L.)

module implemented via transport of intensity equation (TIE)-based phase retrieval and highly multiplex fluorescence imaging module implemented with a flat-field illumination and multispectral detection. The schematic of the Omni-Mesoscope is shown in Fig. 1. Our system achieves an ultralarge FOV at a high resolution through three key hardware elements. First, we adopted an off-the-shelf objective lens (MVPLAPO 2 XC, Olympus) at an NA of 0.5, originally designed for a stereomicroscope with a FOV of centimeters. Second, the mesoscope requires a large-format image sensor with tens of megapixels and a small pixel size, implemented with a cost-effective astronomy camera (ASI294MM pro, ZWO) that has a large-format sensor (IMX 492, ~50 megapixels, 12 times more than scientific complementary metal-oxide semiconductor (sCMOS) and a small pixel size of ~2.3 μm (table S1). Third, we adapted a macro lens (DCR-5320 Pro, Raynox) generally used for photography as the tube lens to achieve an optical magnification of ~7. We prioritized resolution while maximizing the single FOV using low-cost cameras (IMX492) in a single shot. To achieve this, we selected an optimal pixel size that is half of the resolution, based on the Nyquist sampling rate. Last, this cost-efficient combination (~\$4000) provides a final pixel size of ~320 nm with a FOV of ~5 mm² (2.8 mm by 1.8 mm).

A series of images of the fluorescent microspheres is captured along the axial dimension with a step size of 1 μm . Then, we localized each from the 3D fluorescent images, and the fluorescence intensity distribution of each microsphere was used to determine the

point spread function of the imaging system across the FOV. As shown in Fig. 2, the Omni-Mesoscope achieves a lateral submicrometer resolution (700 to 900 nm) and an axial resolution of ~6.2 to 8.7 μm across the entire FOV (2.8 mm by 1.8 mm). At the central region of the FOV, our system maintains a lateral resolution of about 700 nm. Our system can resolve line groups with a spacing of 1.5 μm (fig. S1). Figure 2C shows the field curvature of our system. Initially, the focus shift at the edges of the FOV can reach 8 to 10 μm ; however, this is significantly reduced to less than 1 μm after applying region-based post-refocusing (fig. S3).

The quantitative phase images are reconstructed on the basis of the TIE-based phase retrieval (14) using standard bright-field intensity measurement at two different focal planes ($\pm 2 \mu\text{m}$), which is simple and fast. In addition, our method does not require to modify the existing optical setup for fluorescence imaging compared to the interferometry-based quantitative phase imaging method (15–18). The accuracy of the quantitative phase value and temporal stability were validated using the polystyrene microsphere with a diameter of 2 μm (fig. S2).

Label-free live-cell imaging with TIE-based QPI (QPI-Mesoscope)

We first applied the quantitative phase imaging module of the Omni-Mesoscope for label-free live-cell imaging, where an incubator system was set up with the temperature set to 37°C, humid air, and 5% CO₂. As shown in Fig. 3A, the quantitative phase images of cancer cells

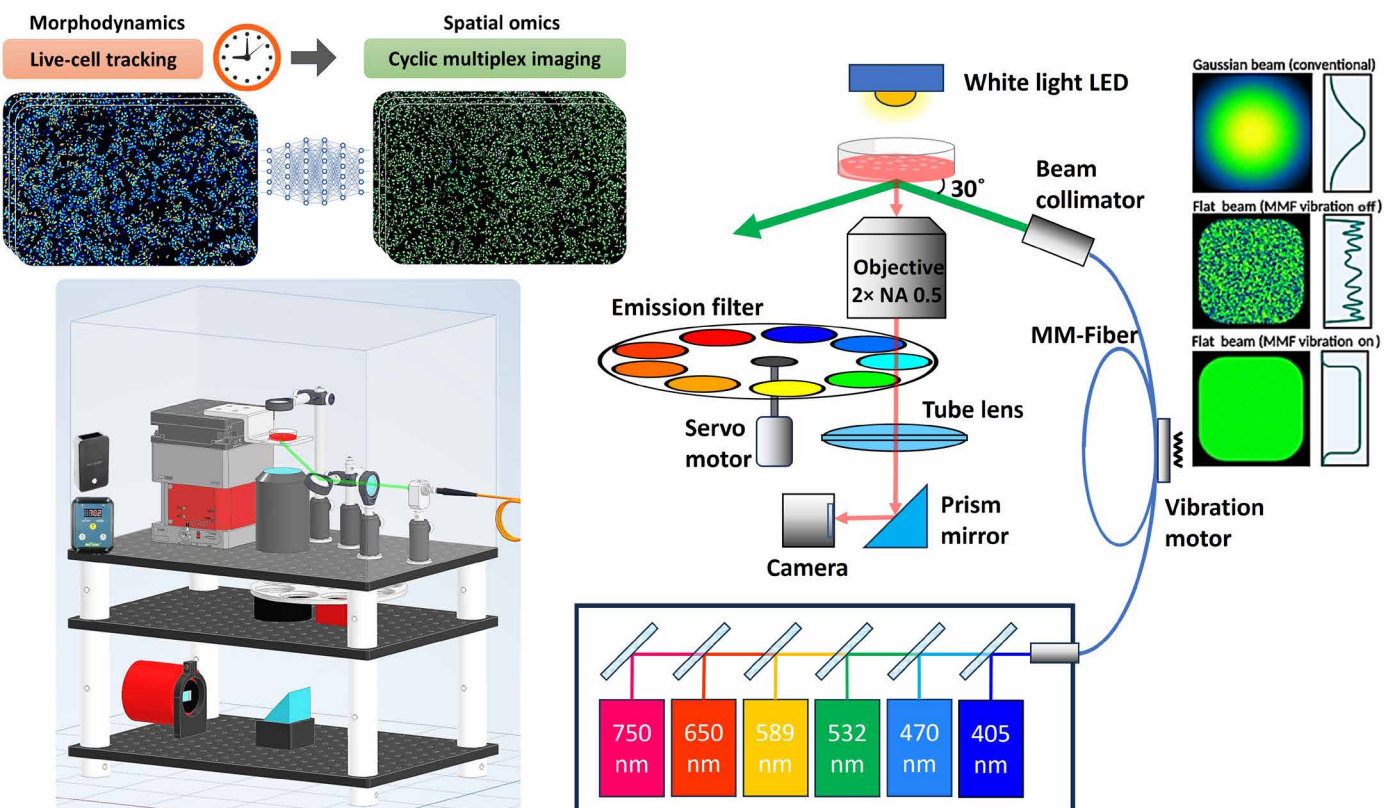


Fig. 1. Schematics of our Omni-Mesoscope system. A collimated light-emitting diode (LED) is used as the illumination beam for quantitative phase imaging. Six diode lasers (405, 470, 530, 589, 650, and 750 nm) coupled to a multimode fiber (MMF) and a high-frequency vibration motor to create uniform flat-field illumination. The illumination light was obliquely introduced from the bottom of the sample with an incident angle of ~60°, which decouples from the detection path. A customized motorized filter wheel with nine band-pass emission filters is used for multiplex fluorescence imaging.

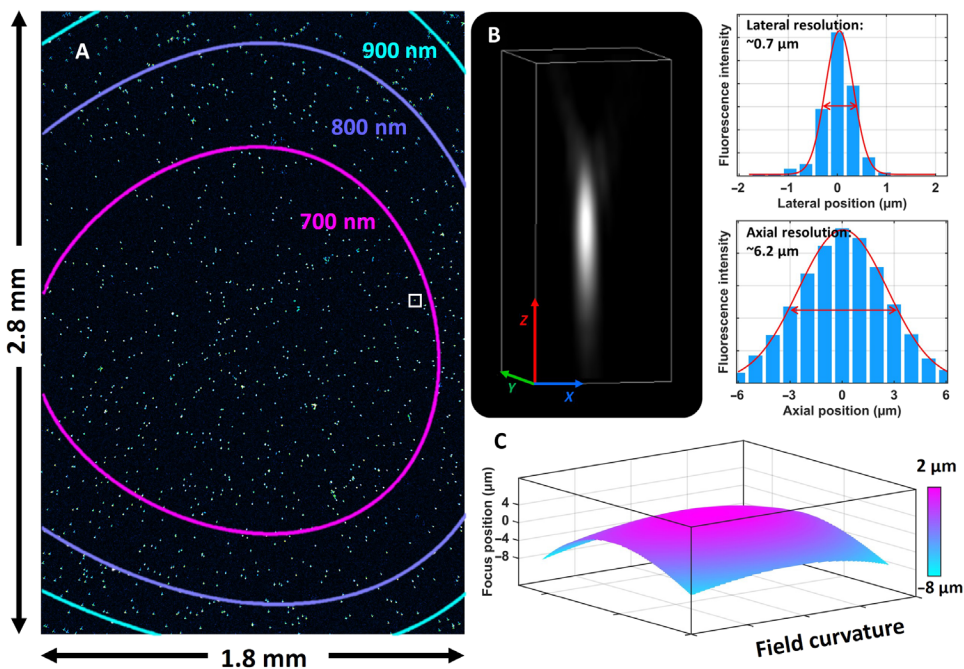


Fig. 2. Performance evaluation of Omni-Mesoscope in resolution and field curvature. (A) The diffraction-limited image of fluorescent microspheres (FluoSpheres, 0.2 μm , 505/515) attached to the surface of a coverslip. To generate a precise and continuous map in resolution, we calculated the resolution at each position by averaging the resolution of tens of beads within a radius of 50 μm . (B) The point spread function (PSF) of the lateral and axial resolution. A Gaussian function is used to fit the PSF of each fluorescent microsphere, and the full width at half maximum of the PSF is defined as the spatial resolution. (C) The field of curvature for Omni-Mesoscope. The focus shift at each position was calculated by averaging the axial position of all beads within a lateral radius of 50 μm .

(SW480) exhibit significantly higher contrast compared to the conventional bright-field images, crucial for the identification of subcellular structures. Leveraging the mesoscale FOV, the QPI-Mesoscope can simultaneously monitor \sim 3000 cells with the ability to capture the heterogeneous cellular dynamics and rare events in a large cell population without the need for scanning or stitching various regions of interest. Moreover, for long-term monitoring, our snapshot imaging feature proves invaluable, as it substantially reduces light exposure, thereby minimizing the effects of phototoxicity (19). As shown in Fig. 3B, our system can track dynamic changes in the cytoskeleton with great subcellular details to visualize large skeletal structural features. We also observed rapid events of mitosis (Fig. 3C) that lasted for about 5 min over a 5-hour observation period.

This quantitative phase image provides enhanced image contrast and is also quantitative in nature (18, 20). Figure 3 (D and E) shows that quantitative assessment of cell dry mass over the course of treatment with a chemotherapy drug, 5-fluorouracil (5-FU). The results reveal that, as cells grow, their morphology gradually becomes less similar over time. In response to 5-FU treatment, the cell morphology undergoes less significant deformation. Similarly, the dry mass gradually increases during cell growth. The treatment with 5-FU also slows down the increase in dry mass, suggesting that the chemotherapy drug reduces protein synthesis during cell growth, consistent with the previous literature report (21).

High-resolution multiplex fluorescence imaging of biological samples (Fluo-Mesoscope)

Next, we evaluated the imaging performance of Omni-Mesoscope for highly multiplex fluorescence imaging on biological samples using cancer cells (SW480). Three subcellular structural components—tubulins,

lamin A/C, and centromeres—were used in this evaluation, as shown in Fig. 4. The results further illustrate the capability of Fluo-Mesoscope to obtain high-resolution fluorescence images over an ultralarge FOV at high throughput while still resolving fine biological structures, such as the two closely adjacent centromeres. As shown in Fig. 4E, the full width at half maximum of a single centromere was measured at 0.7 μm , and the distance between the two adjacent centromeres was at 1.5 μm , confirming the high-resolution imaging capability of Fluo-Mesoscope. These results also agree with the resolution defined using fluorescence microspheres (Fig. 2), further validating the accuracy and consistency of our mesoscopic imaging system.

Omni-Mesoscope links the dynamic cell behaviors of rare events with underlying molecular characteristics

A key advantage of an ultralarge FOV in Omni-Mesoscope is its ability to detect rare dynamic cellular events, which can be linked to their underlying function through high-content molecular profiling *in situ*. This capability was demonstrated through the observation of the response of a cancer cell line, SW480, to the treatment of 5-FU. Using the capability of Omni-Mesoscope for quantitative phase imaging, we simultaneously monitored dynamic morphological changes for 5 hours across a large cell population of a few thousand cells within a single FOV. Within the predominantly slow-moving cell population, we identified a distinct subset that exhibited rapid and significant local movements. These observations are exemplified by a series of snapshot images in Fig. 5 (A1 to A5), with representative videos (movies S1 to S3) providing further illustration. The temporal SD map of phase images, presented in Fig. 5C, identifies a group of cells characterized by significant movement. As shown in Fig. 5B, the quantitative dry mass from the nuclei of

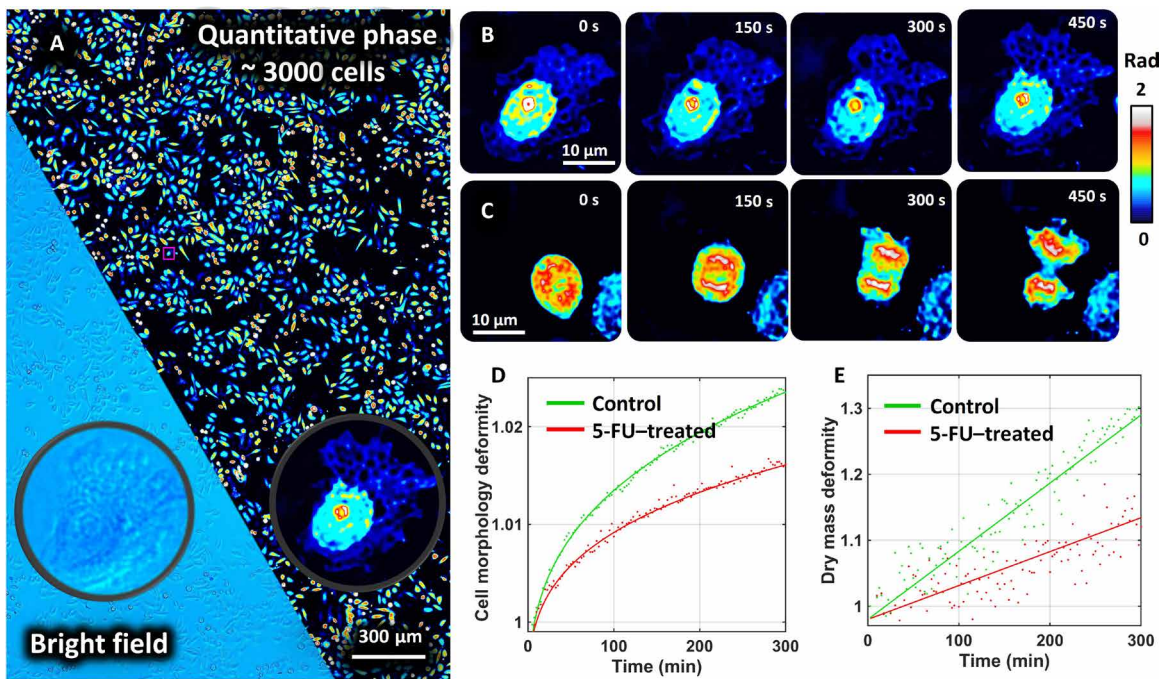


Fig. 3. Label-free live-cell imaging with the quantitative phase imaging module of the Omni-Mesoscope. **(A)** Quantitative phase images of cancer cells in a single FOV, with ~3000 cells. The inset shows the comparison between the bright-field and quantitative phase images. **(B and C)** The dynamic changes of cytoskeleton and mitosis. **(D and E)** The quantification of cell morphological similarity and changes in dry mass in cancer cells without (control) and with the treatment of 5-FU (5-FU-treated) over 5 hours. Cell morphology deformity is quantified as the inverse of the image similarity between QPI images captured over 5 hours and those captured at the initial time point. The total dry mass of a cell is estimated by dividing the product of the quantifiable phase and cell area by the specific refractive index increment (42). Normalized dry mass is calculated by dividing the dry mass of the total cells captured at each time point by that captured at the initial time point.

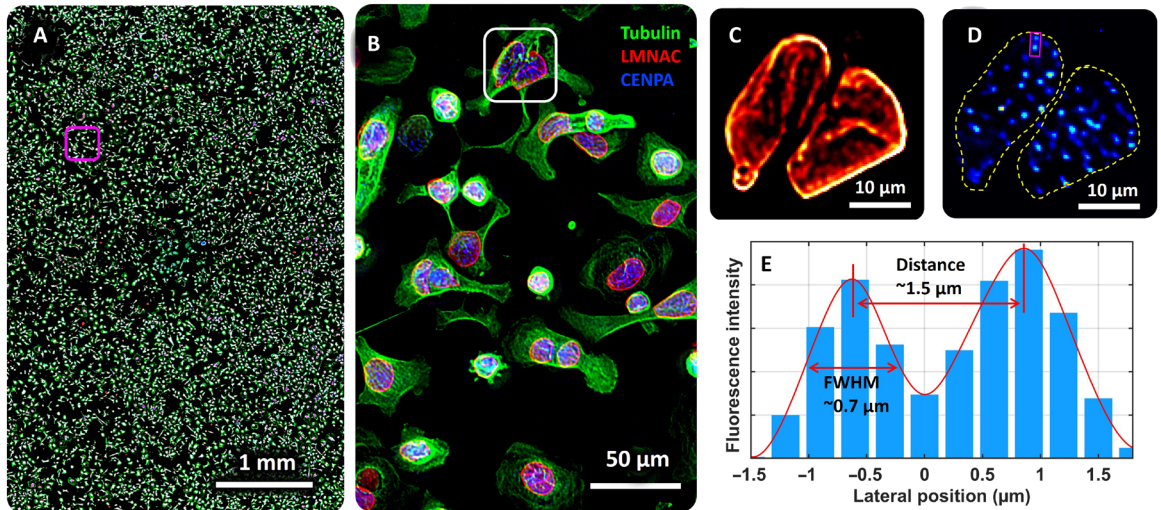


Fig. 4. Performance of Omni-Mesoscope for multiplex fluorescence imaging of biological samples. **(A and B)** Fluorescence images of tubulin, lamin A/C, and centromeres over a large area (2×2 images stitched together) and **(B)** the zoom region of the magenta box from **(A)**. **(C and D)** The zoom region of **(C)** lamin A/C (LMNAC) and **(D)** centromere from the white box in **(B)**. **(E)** The lateral distribution of fluorescence intensity across the two adjacent centromeres (CENPA) in **(D)** was measured at $1.5 \mu\text{m}$ apart with a width of $0.7 \mu\text{m}$. FWHM, full width at half maximum.

these fast-moving cells appears to be almost doubled compared to that of slow-moving cells.

To uncover the function and molecular characteristics of these cells with distinct fast dynamics, we fixed the cells with paraformaldehyde (PFA) after 5 hours of live-cell imaging. As shown in the quantitative phase image (Fig. 5A6), some morphological changes

are expected after fixation, such as cell shrinkage and flattening cytoplasm. However, the cellular morphology and the relative phase difference for different cells and subcellular compartments were largely preserved. Subsequent cyclic immunofluorescence staining and imaging on the Omni-Mesoscope revealed distinct molecular signatures from 14 different molecular markers for the same cells,

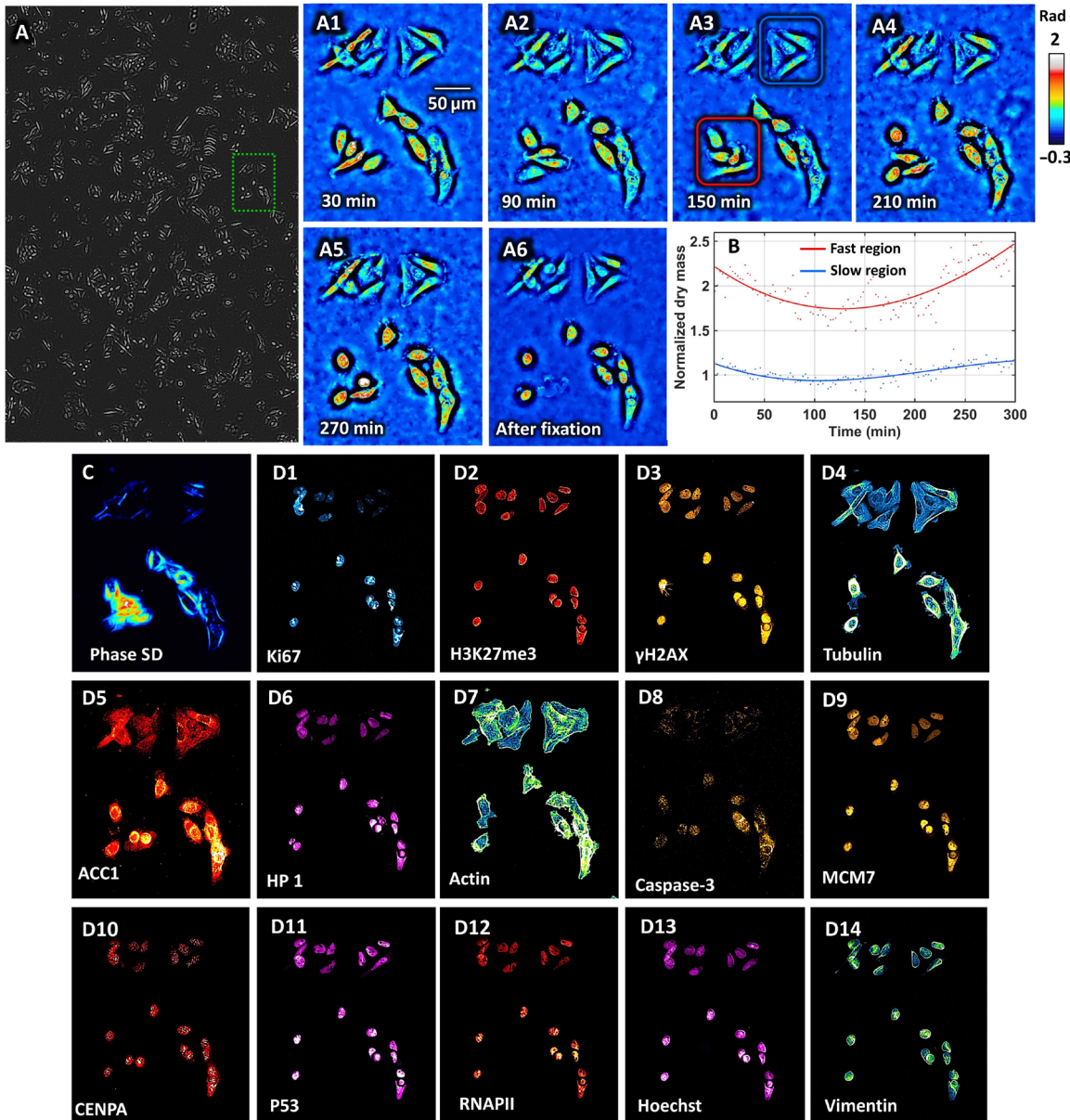


Fig. 5. Correlation of dynamic cellular behaviors with molecular characteristics in SW480 cells treated with 5-FU. (A) The single-FOV quantitative phase image of SW480 cells treated with 35 μ M 5-FU for 3 days. (A1 to A5) Representative sequential snapshot images from the green box in (A), which illustrate the dynamic morphological changes over 5 hours in SW480 cancer cells treated with 5-FU for 3 days, captured within a single FOV encompassing thousands of cells. Most cells display minimal movement, while a subset exhibits significant local motion. (A6) Quantitative phase image after fixation with PFA, serving as a baseline for molecular analysis by preserving cellular structures for detailed examination. (B) The normalized dry mass of four cells in the fast-moving region and slow-moving region in (A3). (C) Temporal SD map of phase images highlighting cells with pronounced movement, indicating areas of active cellular dynamics in response to treatment. (D1 to D14) Fluorescence images of 14 molecular markers in the identified fast-moving cells and adjacent slow-moving cells. These markers include DNA damage (γ H2AX), apoptosis (cleaved caspase-3), proliferation (Ki67 and MCM7), cytoskeletal integrity (actin and tubulin), fatty acid metabolism (ACC1), tumor suppressor (p53), DNA content (H3), heterochromatin (HP1), euchromatin (H3K9ac), centromeres (CENPA), active transcription (phosphorylated RNAPII), and mesenchymal marker (vimentin), providing a comprehensive molecular profile associated with the observed dynamic behaviors.

presented in Fig. 5 (D1 to D14). Notably, the fast-moving cells displayed significantly elevated levels of DNA damage marked by γ H2AX, spread over the entire nucleus. This type of pan-nuclear pattern of γ H2AX without foci indicates excess DNA damage from acute apoptosis (22, 23), distinct from the typical distinguishable γ H2AX foci of DNA damage marker. Further, these cells showed

increased levels of apoptosis (cleaved caspase-3) and proliferation (evidenced by Ki67 and minichromosome maintenance 7 (MCM7), alongside increased expression of cytoskeletal proteins (actin and tubulin), enhanced metabolic activity [Acetyl-CoA-carboxylase 1 (ACC1), a marker for lipid or fatty acid metabolism], and higher DNA content (indicated in H3, HP1, H3K9ac, and centromeres),

while similar levels of vimentin indicate that the cells have not transitioned to a mesenchymal phenotype.

These observations collectively suggest that the fast-moving cells are undergoing significant DNA damage with features of pan-nuclear DNA damage, leading them toward lethal apoptosis in DNA replication stress. However, before succumbing to cell death, these cells show considerable chromatin condensation and marked mobility, supported by a marked increase in metabolic enzymes and cell proliferation proteins. The observed increase in DNA content and dry mass in cells suggests ongoing DNA replication and protein synthesis, yet without subsequent cell division. These results, revealed by the Omni-Mesoscope, provide functional insights into the complex cellular dynamics linked to their response mechanisms to chemotherapy drugs including those rare events.

Furthermore, the Omni-Mesoscope not only facilitates the detection of rare events but also allows a comprehensive analysis of the relationship between these events and the molecular characteristics of individual cells within the entire cell population, all obtained *in situ*. We conducted a uniform manifold approximation and projection (UMAP) analysis (24) for a comprehensive set of 20 markers focusing on the key functions of cell proliferation and epigenetic regulation for ~15,000 cells (SW480), both untreated and treated with 5-FU. The UMAP analysis in Fig. 6 unveiled a distinct, small cluster (cluster 2) of 5-FU–treated cells located on the right side of the visual representation. The UMAP revealed that there is a distinct cell cluster with exceptionally strong signals of γH2AX, indicative of severe pan-nuclear DNA damage. Notably, even within this cluster, there is significant heterogeneity in other morphological and molecular characteristics, such as nuclear size, cell dry mass, DNA content, proliferation status, transcription activities, and epigenetic states, suggesting diverse cellular outcomes in response to 5-FU treatment. Further analysis also revealed a strong correlation between the temporal SD map of phase images from the fast-moving cells and those displaying intense γH2AX signals, as shown in fig. S3. Those fast-moving cells represent a minor fraction (<10%) of the cell population, even among those with excessive DNA damage, emphasizing the rarity of these events.

In addition to significant DNA damage, further analysis of 20 markers reveals that most nuclear proteins are down-regulated in 5-FU–treated cancer cells. This includes H3K27me3 (heterochromatin), EZH2 (the enzyme catalyzing H3K27me3 formation), total H3 (core histone), CENPA (centromeres), HP1 (heterochromatin protein 1), RNA polymerase II (RNAPII; active transcription), along with reduced cell proliferation markers (MCM7 and Ki67). These findings suggest a global reduction in chromatin and transcription activity, likely due to slower cell growth and protein synthesis.

Omni-Mesoscope reveals the formation of polyploidy in drug-resistant cancer cells and their underlying molecular characteristics

The next example highlights the use of the Omni-Mesoscope in characterizing drug-resistant cancer cells. We conducted live-cell imaging of drug-resistant cancer cells that adaptively developed resistance throughout the treatment with increasing concentrations of 5-FU over ~3 months. During a 5-hour imaging session, we monitored the cellular dynamics in these drug-resistant SW480 cells in the presence of 6 μM 5-FU and compared them to the dynamics of the corresponding parent SW480 cancer cells. As the cancer cells adapt and develop chemoresistance, the large FOV provided by

Omni-Mesoscope allowed us to observe the highly heterogeneous dynamic behaviors of these cells. In particular, we observed the formation of polyploid cells through the mechanism of cell engulfing and cell fusion. As shown in Fig. 7 (A1 to A12), a cell was first engulfed into an existing polyploid cell, becoming flattened—a state corroborated by a lower phase value indicative of a thinner cell inside the polyploid cells. This engulfed cell was then divided into two daughter cells within the large polyploid cell (movie S4). Three such cell-engulfing events (movies S4 to S6) were observed over the entire FOV of ~5 mm² with ~1500 cells over 5 hours. In addition, an event involving cell fusion with the polyploid cell was observed (movie S6).

The submicrometer resolution of Omni-Mesoscope enables the detection of functionally significant subcellular dynamics. As illustrated in Fig. 7 (B to D), the quantitative phase image reveals dense puncta within the cell nuclei, which correlate strongly with the corresponding Ki67 fluorescence intensity. This observation indicates that the label-free quantitative phase images can reveal dynamic morphological changes with subcellular details, specifically within nuclear protein Ki67. Smaller dense puncta of Ki67 are evident in the daughter cells derived from the engulfed cell, while larger dense Ki67 puncta are observed in the nuclei of the existing polyploid cells, reflecting their different stages of the cell cycles (25).

Building on these observations, Fig. 8 details the underlying high-content molecular profiling that outlines the specific molecular characteristics of these polyploid cells. These cells exhibit strong stemness (high level of CD44), active fatty acid metabolism (ACC1), significant proliferation (MCM7), and high level of DNA damage (γH2AX). These molecular traits are consistent with the proposed mechanism whereby polyploidization enables cancer cells to survive harmful conditions (26). The previous studies also reported cell cannibalism and cell fusion as possible mechanisms for polyploidy formation (26), which our direct observations using dynamic cellular imaging in a single FOV have confirmed. Further, the quantitative phase images captured highly dynamic cytoskeleton activities, such as cytoskeleton extrusion, which is particularly pronounced in these polyploid cells. The underlying molecular profiling confirms that the extrusion structure comes from both actin and tubulin, suggesting their role in facilitating fast cell movement.

This approach underscores the value of combining label-free dynamic cellular imaging with deep molecular analysis to uncover critical cellular responses to treatment. By facilitating the identification of specific cell subsets undergoing significant stress or damage, such as those highlighted in the UMAP analysis, our methodology that coupled morphodynamic imaging over a large cell population with subsequent high-content molecular profiling, offers a powerful tool for understanding the heterogeneity of cellular responses to pharmacological interventions.

High-throughput 3D volumetric super-resolution imaging of thick tissue (Ex-Mesoscope)

As a versatile imaging platform, our Omni-Mesoscope can also enhance the throughput for highly multiplexed tissue imaging. As shown in fig. S5, with significantly improved FOV and imaging speed, the whole-slide imaging of a tissue section from a small tissue biopsy only requires two images in just a few seconds.

A notable limitation in this ultralarge FOV wide-field optical microscopy lies in its limited 3D sectioning ability, evidenced by an axial resolution of ~6 μm (Fig. 2) in Omni-Mesoscope. The long

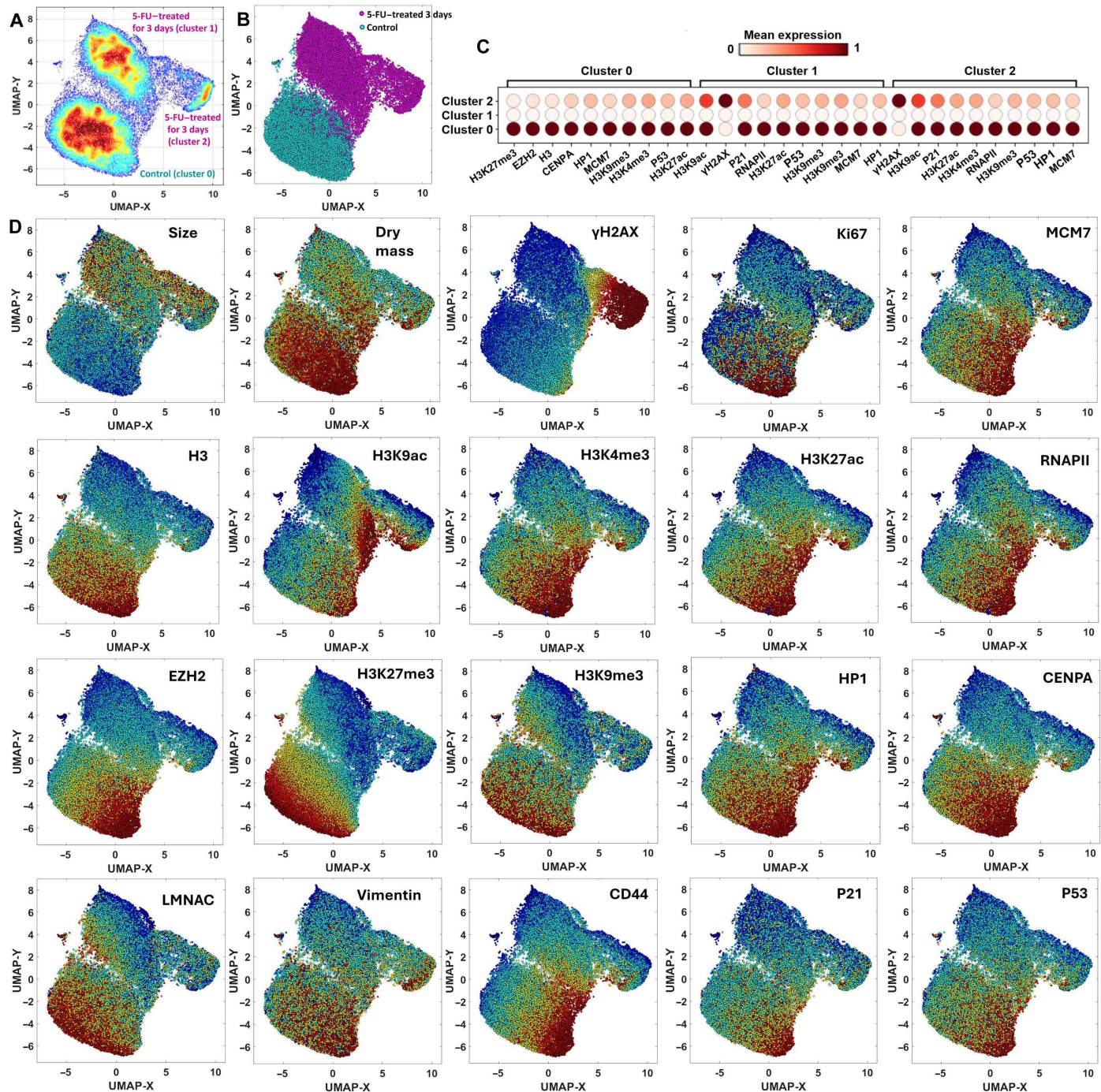
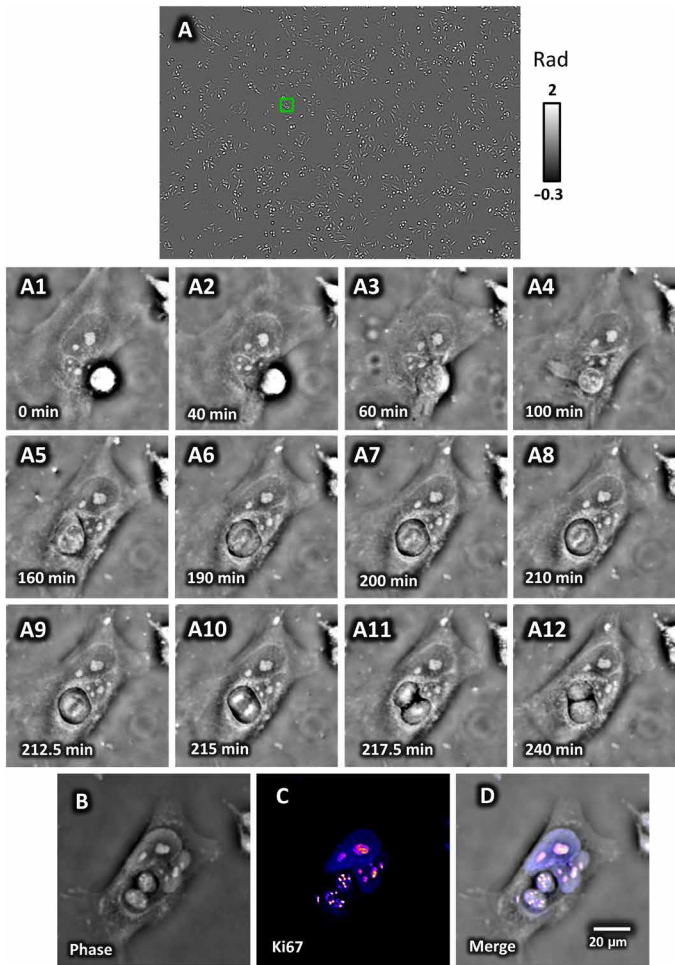


Fig. 6. UMAP analysis for morphological and molecular markers on ~15,000 SW480 cells without (control) and with 5-FU treatment. (A and B) UMAP visualization of the clustered three groups from control cells (SW480) and those treated with 5-FU. (C) Visualization of mean expression level of those proteins with most significant changes between each pair of the clusters. (D) Each panel represents the distribution of the fluorescence intensity for each marker on the clustered UMAP.

depth of field increases the background from thick tissue, which significantly degrades their image quality. To enable 3D volumetric imaging, we have integrated Magnify (27), the state-of-the-art variant of expansion microscopy into our workflow. Expansion microscopy physically enlarges biological specimens, enabling imaging at resolutions surpassing those attainable with conventional microscopy

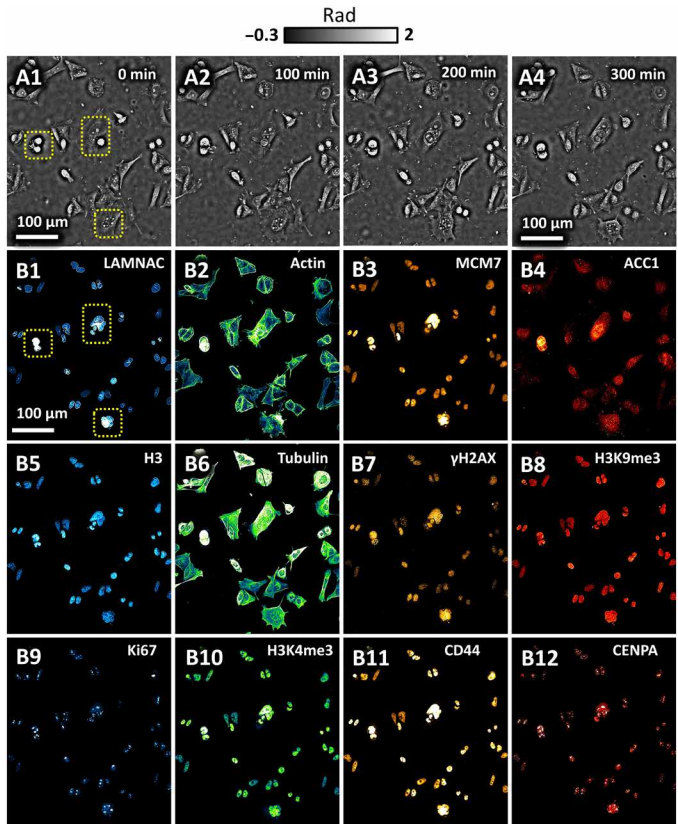
methods. Crucially, the expansion process not only enhances resolution but also significantly mitigates scattering and increases sample transparency.

As shown in Fig. 9A, the 3D volumetric super-resolution images of the expanded samples can be obtained with Omni-Mesoscope (estimated to be ~150-nm lateral resolution and 1.5-μm axial resolution



on the basis of 4.5 expansion ratio), on a 30- μ m-thick section of mouse small intestine tissue. A comparative analysis of tissues, both before expansion (Fig. 9, B and D) and after expansion (Fig. 9, C and E), reveals a significant enhancement in image resolution after expansion. This enhancement allows for the clear visualization of the 3D epithelial cell nuclei in the villi region of the small intestine, along with the precise 3D locations of individual cells. Most notably, the subcellular structure of condensed chromatin foci within each nucleus is also clearly visible.

It is important to note that the Omni-Mesoscope offers a significant increase in imaging throughput for expansion microscopy. This advantage is particularly important given that expanded samples come with a marked volume increase—up to three orders of magnitude after expansion. Consequently, the synergy between the Omni-Mesoscope and expansion microscopy shows tremendous potential for ultrahigh-throughput 3D volumetric super-resolution imaging



of thick tissue samples, to explore complex biological structures with unprecedented clarity and detail at high speed.

DISCUSSION

We present Omni-Mesoscope, a multiscale multimodal imaging system to address the limitations of traditional wide-field optical microscopy. Omni-Mesoscope not only provides high-throughput, high-resolution imaging but also uses label-free quantitative phase imaging to observe cell dynamics across a large cell population. Moreover, it uniquely connects the noninvasive monitoring of morphological dynamics with information-rich molecular characteristics at an unparalleled scale, resolution, and functional insights. Technically, the Omni-Mesoscope achieves a submicrometer lateral resolution for the entire FOV of $\sim 5 \text{ mm}^2$ while using off-the-shelf, cost-effective objective lenses and a large-format camera that together cost around \$4000, making it highly scalable and affordable. In addition, it is compatible with the standard coverslip-based live-cell imaging chamber without the need for a specialized immersion-based imaging chamber.

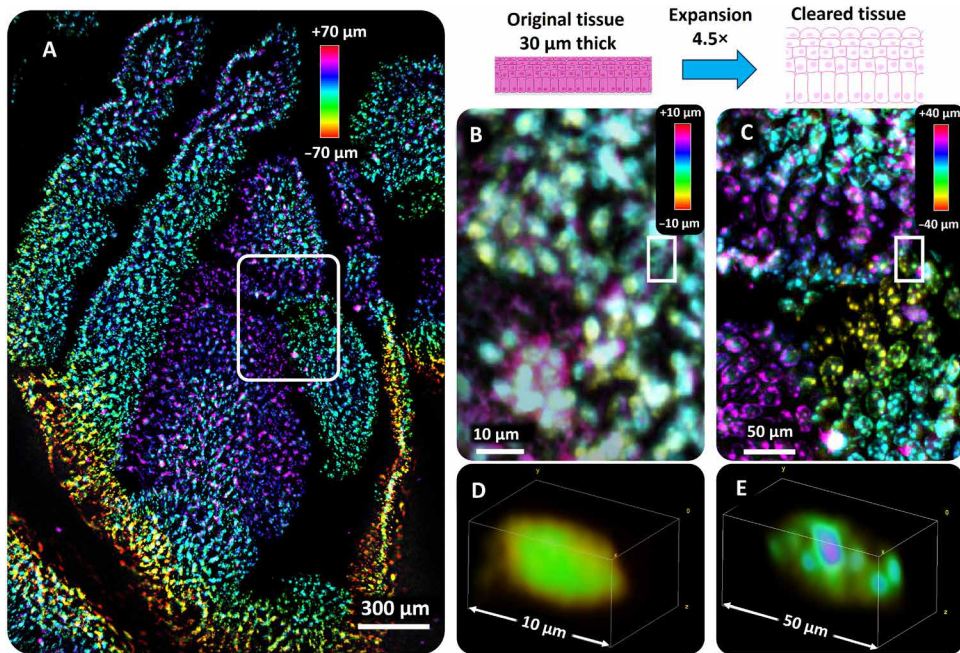


Fig. 9. 3D volumetric super-resolution imaging of thick tissue using the Omni-Mesoscope with expansion microscopy. (A) 3D volumetric super-resolution image of nuclei (4',6-diamidino-2-phenylindole) on an expanded sample (~4.5 \times expansion, 1 \times phosphate-buffered saline) from a 30- μm -thick section of mouse small intestine tissue, obtained using the Omni-Mesoscope. (B and D) Images of the tissue section before expansion, showing the degraded resolution and high background. (C and E) Images of the tissue section after expansion, demonstrating significant improvements in image resolution and 3D sectioning capability of Omni-Mesoscope.

We demonstrate the transformative potential of the Omni-Mesoscope in characterizing cellular responses to chemotherapy and chemoresistance. By capturing specific dynamic events over a large cell population, this mesoscale quantitative phase imaging system reveals dynamic subcellular changes along with their underlying molecular characteristics, marking a significant advancement in cell biology research. Detailed live-cell imaging and molecular profiling provide a comprehensive understanding of cellular responses to 5-FU treatment. The identification of a subset of SW480 cells exhibiting rapid movements and significant DNA damage highlights the potential of Omni-Mesoscope in providing the functional interpretation of specific dynamic cell behaviors. The markedly increased cell mobility could be one enabling capability for those cells to eventually detach from the substrate and undergo apoptosis.

In addition, Omni-Mesoscope facilitates direct observation of cell cannibalism and cell fusion in the formation of polyplloid cells in drug-resistant cancer cells, all within a single FOV. Such dynamic events are then correlated with the molecular traits characteristic of highly aggressive cancer cells such as increased stemness, proliferation, and mobility. Consequently, the integration of mesoscale quantitative phase imaging of cell dynamics together with high-content molecular profiling at submicrometer resolution significantly enhances our ability to dissect the heterogeneity of cellular responses to therapeutic agents and opens new possibilities to probe the complex interplay between cellular dynamics and molecular mechanisms in real time over a large cell population.

The introduction of expansion microscopy within our imaging workflow further enables 3D volumetric super-resolution imaging of thick tissue samples. The Omni-Mesoscope, when coupled with expansion microscopy, shows significantly improved image resolution and 3D sectioning capability on thick tissue sections. It also

addresses a major bottleneck in imaging throughput for 3D imaging of cleared and expanded samples. Future work to further explore the synergy between the Omni-Mesoscope and expansion microscopy will enable ultrahigh-throughput 3D volumetric super-resolution imaging of thick tissue samples to explore complex tissue architecture and molecular characteristics with unprecedented clarity and detail at high throughput.

In conclusion, the Omni-Mesoscope, with its integration of quantitative phase microscopy and highly multiplex fluorescence imaging, presents a significant advancement in our ability to simultaneously capture and analyze the dynamic and molecular essence of cells in unprecedented detail and high molecular content. In the context of the existing mesoscope and light-sheet imaging systems, most target fluorescence imaging with a lateral resolution of 2 to 5 μm (4–10). While the customized mesolens have a similar NA as our system, scaling it up has been a major challenge because of the high cost and labor-intensive nature of manufacturing such a mesolens (28). In contrast to other quantitative phase imaging methods (20), the TIE-based phase imaging method is limited in recovering slowly varying phase information. However, it significantly reduces the complexity of the imaging system while enhancing robustness and speed. Compared to Fourier ptychographic microscopy (29), our Omni-Mesoscope achieves a shorter depth of focus (6 to 8 μm) and a higher temporal acquisition speed of 4 frames per second, offering one-order-of-magnitude improvement in optical sectioning and temporal resolution. It also integrates seamlessly with fluorescence imaging. Our Omni-Mesoscope fills in a gap in the field by simultaneously capturing large-scale temporal dynamics and high-resolution subcellular details over a large cell population while also delivering the high-content molecular characteristics required to decode heterogeneous responses among individual cells in distinct states.

We recognize that the Omni-Mesoscope, in its current form, has limited performance in imaging 3D scattering samples, due to limited axial resolution. Future efforts will address this limitation via parallel scanning, computational imaging, and artificial intelligence-assisted image enhancement. Besides the computation-based aberration correction, the large-field, flatter lens originally designed for telescopes could also be used to physically correct field of curvature aberration. This system opens new avenues for the exploration of biological systems, potentially revolutionizing our approach to diagnostic and therapeutic strategies in the biomedical sciences.

MATERIALS AND METHODS

Instrument development of Omni-Mesoscope

We built the Omni-Mesoscope using cost-efficient off-the-shelf components. In brief, we adopted six cost-efficient industry-grade lasers from Civil Laser to provide a large FOV illumination (30): 405 nm (LSR405CPD-1.2W), 470 nm (LSR470SD-2.5W), 530 nm (LSR530SD-1.2W), 589 nm (LSR589H-1W), 650 nm (LSR650SD-1W), and 750 nm (DL750-T2-1.5W) (28). These six laser lines were combined with dichroic mirrors (T420lpxr, T495lpxr, T556lpxr, T610lpxr, T685lpxr, Chroma), coupled into a multimode fiber (M97L02, Thorlabs) for beam shaping into a flat illumination field (31, 32). The square-core multimode fiber transforms the original beam with an irregular shape into a uniform beam with a square shape. A high-frequency vibration motor (VZ6DL2B0055211, Digikey) was used to reduce the laser speckle and achieve a high uniformity of up to 99%. The laser intensity is electronically controlled by an Arduino board (Arduino Nano Every) with transistor-transistor logic (TTL) mode.

To increase the signal-to-noise ratio, we decoupled the illumination path and detection path, and the light was obliquely introduced from the bottom of the sample with an incident angle of 60°, which is larger than the collection angle of the objective lens (45°). This configuration minimizes scattered and reflected light entering the detector, thus significantly reducing the background noise. A custom motorized filter wheel with nine band-pass emission filters (no. 67-040-438CWL, no. 87-762-510CWL, no. 87-765-549CWL, no. 84-116-572CWL, no. 87-767-615CWL, no. 33-328-631CWL, no. 86-996-676CWL, no. 67-052-692CWL, and no. 84-123-832CWL) was used to switch between different fluorescence imaging channels.

For optimal live-cell imaging, we designed a tabletop incubator with two levels of environmental control to ensure a stable environment. We used a precise inner chamber incubator (TCS-200, AmScope) to maintain the cell chamber at 37°C, and the humid air with 5% CO₂ was injected directly into the chamber incubator. The outer incubator includes a temperature controller (ITC-308, Inkbird) and a high-power heater (WY-H1-B1, YOUCIDI) to maintain the temperature of the whole tabletop space consistently at 37°C with minimal fluctuation (<0.2°C).

Image acquisition procedures

Our Omni-Mesoscope includes two distinct imaging modes: QPI-Mesoscope mode for label-free live-cell imaging and Fluo-Mesoscope mode for multiplex fluorescence imaging. For live-cell imaging mode, we first turn on the incubation system for appropriate temperature (37°C) and CO₂ concentration (5%). Our incubation system achieves a stable condition in about 10 min. We then mount the imaging chamber and start the automatic live-cell imaging. During the imaging process, the Mesoscope automatically finds the focus by

scanning the sample along the axial direction and identifying the focal plane where the captured bright-field images exhibit the lowest normalized variance of the pixels (33). The bright-field images captured at different axial positions at ±2-μm step size are also used for TIE-based quantitative phase reconstruction and refocusing. Live cells were monitored for more than 5 hours with a time interval of 150 s. For multiplex fluorescence imaging mode, a similar bright-field image-based strategy was used for autofocusing. Furthermore, we also captured a 3D stack of fluorescence images for subsequent region-based refocusing. The exposure time was adjusted to achieve a high contrast for each fluorescence channel.

Image processing and statistical data analysis

In this study, three major image processing steps (fig. S4) were used to achieve state-of-the-art image quality.

Flat-field calibration

Two strategies were used to achieve uniform fluorescence imaging. First, a multimode fiber with a square core was used to create uniform illumination, with a vibration motor used to reduce speckle effects (31). This approach enables illumination uniformity of more than 96%. However, the detection efficiency of the objective lens was not uniformly distributed. Second, under uniform illumination, multiple fluorescence images at different positions of the same sample were captured. The average fluorescence intensity at each position was calculated to generate a 2D relative intensity map. Subsequently, a 2D cubic polynomial function was fitted to this map to obtain a 2D normalization map for each pixel. This map calibrated the detection efficiency and produced the final optimized flat-field image with uniformity exceeding 96%.

Region-wise refocusing

Given that all objective lenses exhibit field curvature, region-wise refocusing was implemented to address defocusing issues across a large FOV. Fluorescence microspheres placed on a no. 1.5 coverslip were used to capture 3D image stacks, from which the 3D position of each emitter was retrieved. A 2D cubic polynomial function was then fitted to generate a field curvature map. The full image was divided into 9 × 6 regions, and refocusing was performed by identifying the focal plane within each region. In-focus regions replaced defocused ones to minimize defocus distortions, resulting in a reduction of defocusing distance to ±1 μm.

Background reduction, denoising, and deconvolution

The rolling ball algorithm (implemented with the MATLAB function “imboxfilt”) with a 20-pixel diameter was used to reduce background, leading to an average signal-to-background ratio improvement of two- to fivefold (34, 35). In addition, a Wiener filtering algorithm (implemented with the MATLAB function “wiener2”) was applied to reduce noise and enhance spatial resolution, resulting in a 10 to 20% improvement (34, 36).

Multicycle image registration

We use a customized imaging chamber that uses magnetic forces at multiple positions to adjust the translational and rotational positioning for each imaging cycle. Combined with a closed-loop translation stage (Thorlabs), our mesoscope can locate targets with a precision of 200 μm, which is significantly smaller than the imaging FOV. We then conducted a scanning process over a 5 × 3 FOV grid with a 20% overlap, resulting in a scan region of more than 30 mm². This approach allows us to capture more than 90% of the cells across multiple imaging cycles within the large scanning region. Last, we used a cross-correlation algorithm to stitch the images. We then use

the phase images from each cycle to register the fluorescence images from each cycle using the scale-invariant feature transform.

In brief, quantitative phase images from different cycles are registered using the scale-invariant feature transform (SIFT) method (37), with the image from the first cycle as the reference. SIFT key points are detected independently in each image (38), and feature vectors describing local image gradients around these key points are extracted. Matched features between images are identified by calculating pairwise Euclidean distances between the feature vectors. A 2D similarity geometric transformation matrix is then computed to align the images. All steps, including key point detection, feature extraction, matching, and transformation, are implemented using MATLAB's Image Processing and Computer Vision Toolbox.

UMAP analysis

The UMAP package written in MATLAB (39) is used for data analysis with default parameter setting (`min_dist = 0.3, n_neighbors = 15, metric = Euclidean, randomize = 1`). The data were analyzed using the Scanpy pipeline. First, we applied principal components analysis (PCA) to reduce the dimensionality and calculated the nearest neighbors in the PCA space. We then used UMAP for data visualization and the Leiden algorithm (40) with a resolution of 0.075 for clustering. Last, a *t* test was performed to identify differentially expressed markers within each cluster.

TIE-based quantitative phase imaging (QPI-Mesoscope)

The TIE is essentially an expression of the conservation of energy in optics (14, 41). It establishes a direct mathematical relationship between the spatial phase and the derivative of intensity along the optical axis, enabling the retrieval of quantitative phase values by measuring the phase-induced intensity gradient

$$-k \frac{\partial I(x, y, z)}{\partial z} = \nabla_{\perp} \cdot [I(x, y, z) \nabla_{\perp} \varphi(x, y, z)] \quad (1)$$

where φ is the phase, k is the wave number as $2\pi/\lambda$, λ is the wavelength, I is the image intensity, $\frac{\partial I}{\partial z}$ represents the intensity derivative, ∇_{\perp} is the lateral gradient operator, x and y indicate the lateral spatial coordinate, and z indicates the axial axis. For a phase object under uniform illumination, the intensity along the optical axis is nearly constant, the TIE can be further simplified as a Poisson equation in the following form

$$-\frac{k}{I} \frac{\partial I(x, y, z)}{\partial z} = \nabla_{\perp}^2 \varphi(x, y, z) \quad (2)$$

Then, the spatial phase distribution can be expressed as

$$\varphi(x, y, z) = -\frac{k}{I} \nabla_{\perp}^{-2} \frac{\partial I(x, y, z)}{\partial z} \quad (3)$$

The inverse Laplacian operator (∇^{-2}) can be efficiently calculated by using the fast Fourier transform (\mathcal{F}). Therefore, the phase distribution can be reconstructed as

$$\varphi(x, y, z) = -\frac{k}{I} \mathcal{F}^{-1} \left\{ \frac{u^2 + v^2}{4\pi^2(u^2 + v^2)^2 + \gamma} \mathcal{F} \left[\frac{\partial I(x, y, z)}{\partial z} \right] \right\} \quad (4)$$

where u and v are the spatial frequencies corresponding to the lateral axis, and γ is a regularization parameter to avoid the singularity and remove noise-induced artifacts. Because the axial intensity derivative cannot be measured directly, finite differences are used to

approximate the derivative in practice. In its simplest form, TIE phase retrieval requires only two bright-field intensity images collected at different focuses along the axis dimension

$$\frac{\partial I(x, y, z)}{\partial z} = \frac{I(x, y, \Delta z) - I(x, y, 0)}{\Delta z} \quad (5)$$

where Δz is a small defocus axial distance to provide a good estimation of the intensity derivative.

Dry mass calculation

The total dry mass of a cell is estimated by dividing the product of the phase value and cell area by the specific refractive index increment (42–44). Normalized dry mass is calculated by dividing the dry mass of the total cells captured at each time point by that captured at the initial time point.

Treatment of SW480 cells with 5-FU

The SW480 cells growing on the gelatin-coated coverslip were exposed to 35 μ M 5-FU for durations of 3 days. Subsequently, the cells were imaged using QPI-Mesoscope under live-cell imaging conditions (37°C, 5% CO₂) for 5 hours. Immediately after QPI, the cells were fixed with 4% PFA for 15 min, followed by cyclic fluorescence staining.

Development of drug-resistant SW480 cells

The SW480 cells were gradually exposed to increasing concentrations of 5-FU, starting with 1 μ M, followed by 2 μ M, and then 4 μ M, before reaching a final concentration of 6 μ M. The cells were maintained at each concentration for about 4 weeks. Throughout this period, the culture medium at each concentration was refreshed every 3 days to maintain optimal conditions. Subsequently, the cells were imaged live using QPI-Mesoscope under 37°C and 5% CO₂ for 5 hours. Immediately after imaging, the cells were fixed with 4% PFA for 15 min, followed by cyclic fluorescence staining.

Cyclic immunofluorescence staining

Cultured cells were briefly washed with 1× phosphate-buffered saline (PBS) before being fixed with 4% PFA for 15 min at room temperature (RT). Fixed cells were rinsed with 1× PBS twice before permeabilization with 0.2% Triton X-100 in 1× PBS for 10 min. The cells were incubated with a blocking buffer containing 5% bovine serum albumin in 1× PBS for 30 min at RT. All antibodies were diluted in a blocking buffer. The dilutions and usages of antibodies in each cycle were documented (table S2). The cells from the initial staining or previous bleached cycle were stained with diluted primary or fluorophore-conjugated antibodies at 4°C for 12 hours in a moisture chamber. The cells were then washed with 1× PBS three times.

For indirect immunofluorescence staining, after incubation with primary antibodies, diluted secondary antibodies in blocking buffer were added to the cells for incubation at RT for 2 hours, followed by three washes with 1× PBS. The stained cells were stored in 1× PBS until imaging.

Fluorophore inactivation

After each round of fluorescence imaging, the fluorophores were chemically inactivated by incubation in a bleaching buffer containing 4.5% (w/v) H₂O₂ (Sigma-Aldrich, catalog no. H1009) and 20 mM NaOH (solution made from pellets, Sigma-Aldrich, catalog no. S5881) in 1× PBS for 20 min. The samples were continuously illuminated by two high-power full-spectrum light-emitting diodes

(YUJILEDS-CRI-95, 380 to 1000 nm, 3.6 W) for fluorescence photo-bleaching. After 1 hour of photobleaching, the cells were washed with 1× PBS three times to remove residual oxidation solution before being subjected to a subsequent round of immunofluorescence staining.

Reagents and methods for Magnify

Reagents used in this study included PFA (Sigma-Aldrich, P6148), ethanol (Pharmco, 111000200), xylene (Sigma-Aldrich, 214736), sodium acrylate (SA, AK Scientific, R624; Santa Cruz Biotechnology, sc-236893B), N-dimethylacrylamide (DMAA, Sigma-Aldrich, 274135), acrylamide (AA, Sigma-Aldrich, A8887), *N,N'*-methylenebisacrylamide (BIS, Sigma-Aldrich, M7279), tetramethylethylenediamine (TEMED, Sigma-Aldrich, T9281), 4-hydroxy-2,2,6,6-tetramethylpiperidine 1-oxyl (Sigma-Aldrich, 176141), sodium chloride (NaCl, Sigma-Aldrich, S6191), PBS 10× solution (Fisher Scientific, BP399-1), ammonium persulfate (APS, Sigma-Aldrich, A3678), potassium persulfate (KPS, Sigma-Aldrich, 216224), methacrolein (Sigma-Aldrich, 133035), EDTA (VWR, BDH7830-1), Triton X-100 (Sigma-Aldrich, T8787), Tris Base (Fisher Scientific, BP152-1), proteinase K (Fisher Scientific, EO0491), SDS (Sigma-Aldrich, L3771), urea (Sigma-Aldrich, U5378), and glycine (Sigma-Aldrich, G8898).

SA stock solution preparation

A 50% final concentration was achieved by adding deionized water in multiple increments, stirring continuously to ensure complete dissolution. Adequate time was allowed for complete dissolution before final volume adjustment.

Monomer solution preparation

Composed of 4% (v/v) DMAA, 34% (v/v) SA, 10% (v/v) AA, 0.02% (v/v) BIS, and 1% (w/v) NaCl in 1× PBS, the solution was stored at 4°C until use.

Heat denaturation buffer preparation

This buffer was made of 1% (w/v) SDS, 0.75% (w/v) glycine, 8 M urea, 25 mM EDTA, and 500 mM Tris Base in 2× PBS, adjusted to pH 8.5, and stored at RT.

Deparaffinization of formalin-fixed paraffin-embedded tissue

Formalin-fixed paraffin-embedded pathogen-infected tissue samples underwent deparaffinization through sequential immersion in 2× xylene and 2× 100% ethanol, followed by 95, 70, and 50% ethanol dilutions, and lastly, doubly deionized water. Each step was carried out at RT, lasting 3 min.

In situ polymer synthesis

Before gelation, 0.2 to 0.25% (w/v) APS, 0 to 0.25% (v/v) TEMED, 0.001% (w/v) 4HT, and 0.1 to 0.25% (v/v) methacrolein were added to the monomer solution. After vortexing, the samples were incubated with the gelation solution for 5 to 40 min at 4°C to allow diffusion without premature gelation. Gelation was completed overnight in a humidified chamber at 37°C, using a setup made from spacers cut from no. 1.5 cover glass and a glass slide.

Sample homogenization and expansion with Magnify

After gelation, mouse colon samples were immersed in a denaturant-rich buffer [1% (w/v) SDS, 8 M urea, 25 mM EDTA, and 2× PBS (pH 7.5)] at RT for 30 min. The homogenization was conducted in a pressure cooker at 120°C for 80 min. After homogenization, samples were washed twice with 1% decaethylene glycol monododecyl ether (C12E10) in 1× PBS at 60°C for at least 15 min per wash, followed by two washes at 37°C to remove SDS.

Postexpansion fluorescence staining

Expanded samples were incubated with 4',6-diamidino-2-phenylindole (1 µg/ml) for 10 min before imaging.

Supplementary Materials

The PDF file includes:

Figs. S1 to S5

Tables S1 and S2

Legends for movies S1 to S6

Other Supplementary Material for this manuscript includes the following:

Movies S1 to S6

REFERENCES AND NOTES

- Y. Sasai, Cytosystems dynamics in self-organization of tissue architecture. *Nature* **493**, 318–326 (2013).
- A. Rao, D. Barkley, G. S. França, I. Yanai, Exploring tissue architecture using spatial transcriptomics. *Nature* **596**, 211–220 (2021).
- J. A. Cardin, M. C. Crair, M. J. Higley, Mesoscopic imaging: Shining a wide light on large-scale neural dynamics. *Neuron* **108**, 33–43 (2020).
- Y. Xue, Q. Yang, G. Hu, K. Guo, L. Tian, L. Tian, Deep-learning-augmented computational miniature mesoscope. *Optica* **9**, 1009–1021 (2022).
- I. de Kernier, A. Ali-Cherif, N. Rongeat, O. Cioni, S. Morales, J. Savatier, S. Monneret, P. Blandin, Large field-of-view phase and fluorescence mesoscope with microscopic resolution. *J. Biomed. Opt.* **24**, 036501 (2019).
- A. Glaser, J. Chandrashekhar, J. Vasquez, C. Arshadi, N. Ouellette, X. Jiang, J. Baka, G. Kovacs, M. Woodard, S. Seshamani, K. Cao, N. Clack, A. Recknagel, A. Grim, P. Balaram, E. Turschak, A. Liddell, J. Rohde, A. Hellevik, K. Takasaki, L. E. Barner, M. Logsdon, C. Chronopoulos, S. de Vries, J. Ting, S. Perlmutter, B. Kalmbach, N. Dembrow, R. C. Reid, D. Feng, K. Svoboda, Expansion-assisted selective plane illumination microscopy for nanoscale imaging of centimeter-scale tissues. *eLife* **12**, eP91979 (2023).
- A. E. Cohen, C. A. Werley, M.-P. Chien, Ultrawidefield microscope for high-speed fluorescence imaging and targeted optogenetic stimulation. *Biomed. Opt. Express* **8**, 5794–5813 (2017).
- T. Ichimura, T. Kakizuka, K. Horikawa, K. Seiriki, A. Kasai, H. Hashimoto, K. Fujita, T. M. Watanabe, T. Nagai, Exploring rare cellular activity in more than one million cells by a transscale scope. *Sci. Rep.* **11**, 1–16 (2021).
- T. Ichimura, T. Kakizuka, Y. Sato, K. Itano, K. Seiriki, H. Hashimoto, H. Itoga, S. Onami, T. Nagai, Volumetric trans-scale imaging of massive quantity of heterogeneous cell populations in centimeter-wide tissue and embryo. *eLife* **13**, e93633 (2024).
- R. Shi, X. Chen, J. Deng, J. Liang, K. Fan, F. Zhou, P. Tang, L. Zhang, L. Kong, Random-access wide-field mesoscopy for centimetre-scale imaging of biodynamics with subcellular resolution. *Nat. Photonics* **18**, 721–730 (2024).
- G. McConnell, J. Trägårdh, R. Amor, J. Dempster, E. Reid, W. B. Amos, A novel optical microscope for imaging large embryos and tissue volumes with sub-cellular resolution throughout. *eLife* **5**, e18659 (2016).
- S. Pacheco, C. Wang, M. K. Chawla, M. Nguyen, B. K. Baggett, U. Utzinger, C. A. Barnes, R. Liang, High resolution, high speed, long working distance, large field of view confocal fluorescence microscope. *Sci. Rep.* **7**, 1–10 (2017).
- J. Fan, J. Suo, J. Wu, H. Xie, Y. Shen, F. Chen, G. Wang, L. Cao, G. Jin, Q. He, T. Li, G. Luan, L. Kong, Z. Zheng, Q. Dai, Video-rate imaging of biological dynamics at centimetre scale and micrometre resolution. *Nat. Photonics* **13**, 809–816 (2019).
- C. Zuo, J. Li, J. Sun, Y. Fan, J. Zhang, L. Lu, R. Zhang, B. Wang, L. Huang, Q. Chen, Transport of intensity equation: A tutorial. *Opt. Lasers Eng.* **135**, 106187 (2020).
- M. Mir, J. Rogers, H. Ding, S. Unarunotai, Z. Wang, L. Millet, M. U. Gillette, G. Popescu, Spatial light interference microscopy (SLIM). *Opt. Express* **19**, 1016–1026 (2011).
- P. Marquet, C. Depeursinge, P. J. Magistretti, Review of quantitative phase-digital holographic microscopy: Promising novel imaging technique to resolve neuronal network activity and identify cellular biomarkers of psychiatric disorders. *Neurophotonics* **1**, 020901 (2014).
- L. Durdevic, L. Durdevic, A. R. Ginés, A. Roueff, G. Blivet, G. Baffou, Biomass measurements of single neurites *in vitro* using optical wavefront microscopy. *Biomed. Opt. Express* **13**, 6550–6560 (2022).
- P. C. Chaumet, P. Bon, G. Maire, A. Sentenac, G. Baffou, Quantitative phase microscopies: Accuracy comparison. arXiv:2403.11930 [physics.optics] (2024).
- M. M. Frigault, J. Lacoste, J. L. Swift, C. M. Brown, Live-cell microscopy—tips and tools. *J. Cell Sci.* **122**, 753–767 (2009).
- Y. K. Park, C. Depeursinge, G. Popescu, Quantitative phase imaging in biomedicine. *Nat. Photonics* **12**, 578–589 (2018).
- E. R. Polanco, T. E. Moustafa, A. Butterfield, S. D. Scherer, E. Cortes-Sanchez, T. Bodily, B. T. Spike, B. E. Welm, P. S. Bernard, T. A. Zangle, Multiparametric quantitative phase imaging for real-time, single cell, drug screening in breast cancer. *Commun. Biol.* **5**, 1–12 (2022).
- S. De Feraudy, I. Revet, V. Bezrookove, L. Feeney, J. E. Cleaver, A minority of foci or pan-nuclear apoptotic staining of γH2AX in the S phase after UV damage contain DNA double-strand breaks. *Proc. Natl. Acad. Sci. U.S.A.* **107**, 6870–6875 (2010).

23. C. J. Kim, A. L. Gonye, K. Truskowski, C. F. Lee, Y. K. Cho, R. H. Austin, K. J. Pienta, S. R. Amend, Nuclear morphology predicts cell survival to cisplatin chemotherapy. *Neoplasia* **42**, 100906 (2023).
24. L. McInnes, J. Healy, N. Saul, I. Großberger, UMAP: Uniform manifold approximation and projection. *J. Open Source Softw.* **3**, 861 (2018).
25. X. Sun, P. D. Kaufman, Ki-67: More than a proliferation marker. *Chromosoma* **127**, 175–186 (2018).
26. H. Was, A. Borkowska, A. Olszewska, A. Klemba, M. Marciniak, A. Synowiec, C. Kieda, Polyploidy formation in cancer cells: How a Trojan horse is born. *Semin. Cancer Biol.* **81**, 24–36 (2022).
27. A. Klimas, B. R. Gallagher, P. Wijesekara, S. Fekir, E. F. DiBernardo, Z. Cheng, D. B. Stolz, F. Cambi, S. C. Watkins, S. L. Brody, A. Horani, A. L. Barth, C. I. Moore, X. Ren, Y. Zhao, Magnify is a universal molecular anchoring strategy for expansion microscopy. *Nat. Biotechnol.* **41**, 858–869 (2023).
28. G. McConnell, Where next for the Mesolens? *Wiley Analytical Science* (2020); <https://analyticalscience.wiley.com/content/article-do/next-mesolens>.
29. G. Zheng, R. Horstmeyer, C. Yang, Wide-field, high-resolution Fourier ptychographic microscopy. *Nat. Photonics* **7**, 739–745 (2013).
30. H. Ma, R. Fu, J. Xu, Y. Liu, A simple and cost-effective setup for super-resolution localization microscopy. *Sci. Rep.* **7**, 1–9 (2017).
31. H. Ma, Y. Liu, Super-resolution localization microscopy: Toward high throughput, high quality, and low cost. *APL Photonics* **5**, 60902 (2020).
32. H. Ma, M. Chen, P. Nguyen, Y. Liu, Toward drift-free high-throughput nanoscopy through adaptive intersection maximization. *Sci. Adv.* **10**, 7765 (2024).
33. Z. Bian, C. Guo, S. Jiang, J. Zhu, R. Wang, P. Song, Z. Zhang, K. Hoshino, G. Zheng, Autofocusing technologies for whole slide imaging and automated microscopy. *J. Biophotonics* **13**, e202000227 (2020).
34. H. Ma, Y. Liu, “Super-resolution imaging through single-molecule localization” in *Biomedical Optical Imaging*, J. Xia, R. Choe, Eds. (AIP Publishing LLC, 2021), pp. 4–1–4–26.
35. H. Ma, W. Jiang, J. Xu, Y. Liu, Enhanced super-resolution microscopy by extreme value based emitter recovery. *Sci. Rep.* **11**, 1–10 (2021).
36. H. Ma, J. Xu, Y. Liu, WindSTORM: Robust online image processing for high-throughput nanoscopy. *Sci. Adv.* **5**, eaaw0683 (2019).
37. D. G. Lowe, Distinctive image features from scale-invariant keypoints. *Int. J. Comput. Vis.* **60**, 91–110 (2004).
38. H. Bay, T.uytelaars, L. Van Gool, “SURF: Speeded Up Robust Features” in *Computer Vision – ECCV 2006. Lecture Notes in Computer Science (including subseries Lecture Notes in Artificial Intelligence and Lecture Notes in Bioinformatics)*, A. Leonardis, H. Bischof, A. Pinz, Eds. (Springer, 2006), vol. 3951 LNCS, pp. 404–417.
39. C. Meehan, J. Ebrahimian, W. Moore, S. Meehan, Uniform Manifold Approximation and Projection (UMAP), MATLAB Central File Exchange (2022); www.mathworks.com/matlabcentral/fileexchange/71902-uniform-manifold-approximation-and-projection-umap.
40. V. A. Traag, L. Waltman, N. J. van Eck, From Louvain to Leiden: Guaranteeing well-connected communities. *Sci. Rep.* **9**, 1–12 (2019).
41. D. Paganin, A. Barty, A. Roberts, K. A. Nugent, Quantitative optical phase microscopy. *Opt. Lett.* **23**, 817–819 (1998).
42. Y. Liu, S. Uttam, Perspective on quantitative phase imaging to improve precision cancer medicine. *J. Biomed. Opt.* **29**, S22705–1 (2024).
43. R. Barer, Determination of dry mass, thickness, solid and water concentration in living cells. *Nature* **172**, 1097–1098 (1953).
44. G. Popescu, Y. K. Park, N. Lue, C. Best-Popescu, L. Deflores, R. R. Dasari, M. S. Feld, K. Badizadegan, Optical imaging of cell mass and growth dynamics. *Am. J. Physiol. Cell Physiol.* **295**, 538–544 (2008).

Acknowledgments

Funding: This work was supported by National Institutes of Health grant R01CA254112 (Y.L.), National Institutes of Health grant R01CA232593 (Y.L.), National Institutes of Health grant R21CA259787 (Y.L.), National Institutes of Health grant P41EB031772 (Y.L.), National Institutes of Health grant R01EB035890 (Y.Z.), National Institutes of Health grant RF1MH129267 (Y.Z.), and the Charles E. Kaufman Foundation (Y.Z.). **Author contributions:** Conceptualization: H.M., J.X., and Y.L. Data curation: H.M. Formal analysis: H.M. and Y.Y. Investigation: H.M., J.X., and Y.Z. Methodology: H.M., J.X., and Y.Z. Funding acquisition: Y.L. Resources: H.M., J.X., and Y.Z. Software: M.C. and H.M. Supervision: Y.L. Validation: J.X. and H.M. Visualization: H.M. and M.C. Project administration: Y.L. Writing—original draft: H.M. and Y.Z. Writing—review and editing: H.M., Y.Z., and Y.L. **Competing interests:** H.M. and Y.L. are inventors on a provisional US patent application related to this work by the University of Illinois Urbana-Champaign (no. 63/670,569, filed 12 July 2024). Y.Z. is an inventor on patents and patent applications related to this work filed by Carnegie Mellon University (patent no. 11,802,822, filed 3 December 2020, published 31 October 2023; patent applications 18/267,134, filed 15 December 2021, published 15 February 2024; 17/251,855, filed 14 September 2019, published 19 August 2021). The authors declare that they have no other competing interests. **Data and materials availability:** All data needed to evaluate the conclusions are shown in the paper and/or the Supplementary Materials. The raw image data are deposited at <https://doi.org/10.5061/dryad.t76hdr88t> for free download.

Submitted 16 May 2024

Accepted 12 September 2024

Published 16 October 2024

10.1126/sciadv.adq5009